Journal of Materials Chemistry B

ROYAL SOCIETY OF CHEMISTRY

PAPER

View Article Online
View Journal

Cite this: DOI: 10.1039/d6tb00052e

Mechanistic model for improved performance of mRNA–LNPs formulated under turbulent mixing conditions

Richard Mosesso,[a] Katie Randall,[a] Amita Vaidya, *[a] Jackie Tang, [a] Trent Northen,[a] Aurélie Deliot,[b] Mengwei Sun, [a] Rebecca Goldman,[a] Adam Lyons,[a] Lingyun Liu, [a] Shrirang Karve [a] and Frank DeRosa[a]

mRNA delivery using lipid nanoparticles (LNPs) has become a cornerstone of modern biological therapeutics. During the formulation of LNPs, uniform mixing of LNP components is critical to ensuring desirable functional properties. This study employs simple bi-directional T-mixing of lipids in ethanol with mRNA in buffer to evaluate the effects of mixing chamber turbulence on mRNA–LNP biophysical attributes and develops a mechanistic model relating the mixing processes to biological performance. LNPs encapsulating hEPO mRNA formulated under turbulent mixing conditions with ionizable lipid OF-02 demonstrate higher hEPO expression than those formulated under laminar mixing conditions *via* two routes of administration in an *in vivo* mouse model. By measuring LNP zeta potential, fusogenicity, and lipid fluidity as functions of pH, we propose a hypothetical model for increased pH-sensitivity of the turbulently formulated LNPs, presumably resulting in improved intracellular release of mRNA. Unique profiles measured by small-angle X-ray scattering (SAXS) and greater homogeneity observed by cryo-TEM for LNPs formulated under turbulent mixing conditions further support this model. Increased serum protein binding for these turbulently mixed mRNA–LNPs suggests an additional mode of action involving receptor-mediated uptake following systemic delivery. A follow-up study with LNPs made with reduced lipid : mRNA mass ratios indicates that turbulent mixing may preserve LNP function with lower lipid load, compared to LNPs made with higher lipid load under laminar flow conditions. Altogether, these findings underscore important connections between LNP performance and formulation process, offering valuable insights for optimization of mRNA–LNP formulations.

Received 6th January 2026,
Accepted 16th March 2026

DOI: 10.1039/d6tb00052e

rsc.li/materials-b

Introduction

Innovations in lipid nanoparticle (LNP) formulations and processes have revolutionized the field of nucleic acid delivery. The development and subsequent FDA approval of *Onpattro* (patisiran) served as one of the earliest clinical demonstrations of the potential of RNA–LNP therapeutics, using siRNA to treat hereditary transthyretin-mediated amyloidosis.[1] This was followed by the widespread development and deployment of COVID-19 vaccines by Pfizer-BioNTech and Moderna, which further demonstrated the utility of LNPs for delivery of protein-coding mRNAs.[2–4] These clinical successes have helped establish LNPs as a leading platform for delivery of nucleic acid therapeutics.

Among the various types of nucleic acid cargos, mRNA–LNPs have become a major focus due to their flexibility, manufacturability, potency, and rapid development timelines.[5] While mRNA is inherently unstable and susceptible to enzymatic degradation, its encapsulation within LNPs has the multiplexed role of protecting against degradation, as well as improving circulation in the body and facilitating delivery into cells.[6,7] However, vaccine and therapeutic applications of mRNA–LNPs still face several limitations, which have motivated ongoing research and development efforts to improve RNA chemistry,[8,9] design novel ionizable lipids with lipid composition optimization,[10] and refine organ and cell targeting.[11–13] Another area of focus has been the process of formulation itself, which plays a central role in determining the physicochemical and functional properties of LNPs.[10,14]

mRNA–LNP formulations are typically produced by mixing the mRNA payload in an acidic aqueous buffer with lipids dissolved in an organic solvent like ethanol, resulting in nanoprecipitation and encapsulation of the mRNA cargo by

[a] *mRNA Center of Excellence, Sanofi, 200 West St, Waltham, MA 02451, USA. E-mail: amita.vaidya@sanofi.com*
[b] *VCDS Department, Sanofi Pasteur, 1541 Av. Marcel Mérieux, Marcy-L'Étoile, 69280, France*

the LNP components.[7,14] A diverse range of formulation parameters—including flow rates, flow rate ratios, mixing device designs and dynamics (*e.g.* tubing, chips, *etc.* of varying dimensions), geometric mixing angles, lipid compositions, and buffer conditions—can influence the resulting nanoparticle properties, such as particle size, surface charge, encapsulation efficiency, lipid packing, particle heterogeneity, and stability.[15–19] Across a range of scales, microfluidic mixing is commonly used due to its ability to promote rapid and uniform mixing.[20–23] However, in the context of GMP manufacturing and commercialization where microfluidic platforms may be challenging, focused efforts on efficient scalable mixing processes to ensure uniform mixing of formulations are merited. Faster mixing speeds and mixing chamber designs are associated with more turbulent flow, which can yield smaller and more uniform LNPs.[24–26] In this study, we have employed a simple bi-directional T-mixing process employing pulseless flow and a constant flow rate ratio, as described previously.[27] We quantify the turbulence in the mixing chamber with a dimensionless metric "Reynolds number" (Re) by idealizing the flow as the sum of the two opposing flowrates as unidirectional flow in a pipe with the same diameter as the T-mixer. For the purposes of this study, Re values for different combinations of flow rates and T-sizes were calculated using eqn (1), where ρ is density of the resultant solution (kg m^{-3}), V is sum of the linear velocities of the opposing streams (m s^{-1}), L is the nominal diameter of the T-mixer (m), and μ is the viscosity, approximating bulk viscosity for dynamic viscosity (kg m s^{-1}). To generate LNPs at different Re, the T-diameter was varied from 1/8 inch to 1/16 inch, and total flow rates were varied from 62.5 mL min^{-1} to 625 mL min^{-1}, as described in Table S1. Conflicting reports exist on the specific ranges of Re that best describe fluid flow as being "laminar," "transitional," or "turbulent"; however, the degree of turbulence as represented by Re is a continuous spectrum.[28] In this report, we have chosen to refer to $Re < 2000$, $2000 < Re < 4000$, and $Re > 4000$ by those terms, respectively.

$$\mathrm{Re} = \frac{\rho \times V \times L}{\mu} \quad (1)$$

Eqn (1). Formula used to calculate Reynolds Number (Re).

Although previous studies have examined and reported on the impacts of formulation mixing parameters on physical characteristics of mRNA–LNPs, few have directly connected these formulation attributes to functional outcomes like *in vivo* expression or therapeutic efficacy.[24,29,30] In this study, we aim to address this limitation by investigating how turbulence in the mixing chamber (represented by Re) influences LNP performance. Using the model lipid OF-02, a potent ionizable lipid for nucleic acid delivery,[31] we show that LNPs formulated at higher Re typically yield increased expression *in vivo via* enzyme-linked immunosorbent assay (ELISA) of human erythropoietin protein (hEPO) expressed in mice administered by intramuscular (I.M.) and intravenous (I.V.) dosing. We further describe a mechanistic model to better understand the structure–activity relationship between this increased protein expression and LNP characteristics by performing a broad set of biophysical characterizations, including basic measurements of particle size (*via* dynamic light scattering, DLS), and encapsulation efficiency (*via* Ribogreen assay), as well as surface charge (zeta potential), membrane fluidity (using the lipophilic Laurdan reagent), fusion with model endosomes, small-angle X-ray scattering (SAXS), asymmetric flow field-flow fractionation combined with multi-angle light scattering (AF4–MALS), cryo-transmission electron microscopy (Cryo-TEM), and serum protein binding (*via* Quartz crystal microbalance with dissipation monitoring, or QCM-D). Through these analytical assessments, we demonstrate that LNPs formulated at higher Re are more fusogenic at early endosomal pH, and have lower surface charge, greater lipid fluidity, and distinct SAXS profiles at pH 4.5, highlighting underlying structural differences that may lead to improved performance. We further demonstrate that LNPs formulated at higher Re have greater binding of serum proteins, especially apolipoprotein E3 (Apo-E3), which is particularly important for receptor-mediated uptake of systemically dosed LNPs.[32] In a follow-up investigation, we also explore how reducing the mass ratio of lipid : mRNA may be partially offset by increasing Re, offering a potential strategy for optimizing formulations with lower lipid load. Taken together, this work contributes to a deeper understanding of how mixing dynamics shape mRNA–LNP structure and function and provides mechanistic insights into formulation–performance relationships.

Materials & methods

Lipids and reagents

OF-02(3,6-Bis[4-[bis[(9*Z*,12*Z*)-2-hydroxy-9,12-octadecadien-1-yl]-amino]butyl]-2,5-piperazinedione) was purchased from Seqens (Devens, MA). DOPE (1,2-di-(9*Z*-octadecenoyl)-*sn-glycero*-3-phosphoethanolamine), DOPC (1,2-dioleoyl-*sn-glycero*-3-phosphocholine), DOPS (1,2-di-(9*Z*-octadecenoyl)-*sn-glycero*-3-phospho-L-serine – sodium salt), 18 : 1 NBD-PE (1,2-dioleoyl-*sn-glycero*-3-phosphoethanolamine-*N*-(7-nitro-2-1,3-benzoxadiazol-4-yl) – ammonium salt), and 18 : 1 Liss Rhod-PE (1,2-dioleoyl-*sn-glycero*-3-phosphoethanolamine-*N*-(lissamine rhodamine B sulfonyl) – ammonium salt) were purchased from Avanti. Cholesterol was purchased from Sigma. DMG-PEG_{2k} (1,2-dimyristoyl-*rac-glycero*-3-methoxypolyethylene glycol-2000) was purchased from Sunbright (Hyogo, Japan). PeproTech® recombinant human apolipoprotein-E3 (Apo-E3) and recombinant human apolipoprotein-A1 (Apo-A1) were purchased from Thermo Fisher. Cellastim S™ recombinant human albumin was purchased from Sigma-Aldrich.

Preparation of mRNA–LNPs

DMG-PEG_{2k}, ionizable lipid, cholesterol, and DOPE were weighed and dissolved separately in 100% ethanol (Fisher Scientific). The lipids were then mixed and diluted with additional ethanol to constitute a lipid mixture with molar ratios of 1.5 : 40 : 28.5 : 30 mol% of DMG-PEG_{2k} : ionizable lipid : cholesterol : DOPE, respectively, at appropriate concentrations and volumes for the desired lipid : mRNA mass ratio (28 mg total lipid per 1 mg mRNA for most formulations in this study).

To constitute the aqueous phase, hEPO mRNA (synthesized and purified in-house) was diluted to 0.0833 mg mL^{-1} in pH 4.0 buffer containing 1 mM citrate buffer (Boston Bioproducts) and 150 mM sodium chloride (Boston Bioproducts). The aqueous and organic phases were mixed in a 4 : 1 flow rate ratio (aqueous : organic) *via* gear pumps (Cole-Palmer) using Masterflex nylon T-connectors (Avantor) with nominal diameters of 1/8″, 3/32″, or 1/16″ depending on the desired Re, as described in Karve *et al.*[27] The T-mixed product was then buffer exchanged *via* tangential flow filtration using a Pellicon 2 Mini membrane (Millipore). The T-mixed product was first concentrated to a working volume of approximately 75 mL prior to six diafiltration volumes of 20% ethanol (v/v) followed by eight diafiltration volumes of 10% trehalose (w/v) (Boston Bioproducts). The final product was collected and concentrated using Amicon ultracentrifugal filters (100 kDa MWCO; sigma) prior to sterile filtration and storage at −80 °C.

mRNA encapsulation

Quant-iT RiboGreen RNA Assay Kit (Invitrogen) was used to assess mRNA encapsulation efficiency following the manufacturer's instructions. All dilutions were performed in 10× TE (Boston Bioproducts). Briefly, LNPs were diluted 1 : 100 and further diluted into tubes containing additional 10× TE ± 0.2% Triton-X 100 (Fisher) prior to the addition of an equal volume of Ribogreen reagent (diluted 0.005× in 10× TE). After a brief incubation, fluorescence at 520 nm was measured on a SpectraMax M5 microplate reader (Molecular Devices, San Jose, CA) using an excitation wavelength of 480 nm. The mRNA encapsulation efficiency (EE%) was calculated using the following equation:

$$\text{Encapsulation efficiency (\%)} = \frac{\text{Total mRNA } (\text{mg mL}^{-1}) - \text{Free mRNA } (\text{mg mL}^{-1})}{\text{Total mRNA } (\text{mg mL}^{-1})} \times 100\%$$

Particle size and zeta potential

Particle size and zeta potential of the LNPs were characterized using a Zetasizer Pro (Malvern, UK). The particle size, measured *via* dynamic light scattering (DLS), is reported as the intensity-weighted mean hydrodynamic diameter in 10% trehalose. To measure zeta potential, LNPs were first diluted to 0.5 mg mL^{-1} mRNA in 10% trehalose, prior to diluting 1 : 100 with 1 mM potassium chloride (sigma) in 5 mM citrate-phosphate buffer (Boston Bioproducts) at the specified pH. A minimum of 25 runs were collected and averaged per measurement, and three separate measurements were averaged to give each reported value.

In vivo protein expression

Ethical statement: All *in vivo* experiments and assays of hEPO expression were performed at Alpha Preclinical facility (Worcester, MA), according to animal protocols approved by the Institutional Animal Care and Use Committee (IACUC).

For intramuscular administration, 30 μL of LNPs at 0.05–0.1 μg mRNA per animal were injected into the right gastrocnemius muscle of female BALB/c mice (6–8 weeks old, n = 4). For intravenous injection, 0.05–0.1 mg kg^{-1} of mRNA in LNPs were injected *via* tail vein of female BALB/c mice (6–8 weeks old, n = 4). All LNPs were diluted and dosed based on total mRNA concentration. For I.M. route of administration, blood samples were collected 6 hours post-injection, and for I.V. route of administration, blood samples were collected 24 hours post-injection. hEPO levels in the sera were measured using ELISA, according to the manufacturer's instructions. For each individual study, data from all cohorts was normalized to data from cohort with the lowest-Re LNP formulation.

AF4-MALS, DLS, and differential refractometer (AF4-MALS-DLS-dRI)

An Agilent 1260 Infinity II HPLC system was coupled to an in-line AF4-MALS-DLS-dRI system. The AF4-MALS-DLS-dRI system was comprised of an Eclipse Long Channel fitted with a 10 kDA regenerated cellulose membrane and a 400 μm laminated spacer. The in-line detectors included the DAWN MALS integrated with WyattQELS dynamic light scattering and an Optilab differential refractometer. For all samples, the dn/dc was set to 0.16 mL g^{-1} and the mobile phase refractive index set to 1.331. Baselines of blanks were subtracted from all samples; band broadening and delay volumes between the detectors were determined using bovine serum albumin (BSA). mRNA–LNPs (5 μL at 0.5 mg mL^{-1}) were injected onto the Eclipse long channel. The channel flow was set to 1.0 mL min^{-1}, the injection flow at 0.20 mL min^{-1}, and detector flow at 0.50 mL min^{-1}, using 1× PBS as a mobile phase. The focusing position was set to 13%, and focusing was implemented for 5 min utilizing a cross-flow of 0.75 mL min^{-1}. Elution was carried out using an initial cross-flow of 1.0 mL min^{-1}, which exponentially decreased over 40 minutes to 0.5 mL min^{-1}.

Liposome fusion assay

The liposome fusion assay was conducted using a modified protocol from Liu *et al.*[33] Liposomes were prepared by thin film rehydration. Lipid films were first prepared by dissolving DOPE, DOPC, DOPS, NBD-PE, and Liss Rhod-PE in chloroform in molar ratios of 48 : 25 : 25 : 1 : 1, respectively, prior to evaporation of the solvent under vacuum on a rotary evaporator in a water bath at 37 °C. The lipid film was left in a desiccator overnight under vacuum to remove any residual solvent. The film was then hydrated in water to a concentration of 12.5 mM total lipid, followed by 30 min sonication in a 37 °C water batch. Liposomes were then extruded using two gas-tight syringes (Avanti) and a mini-extruder (Avanti) 6 times back and forth between a 0.2 μm membrane (Cytiva), followed by another 6 cycles with a 0.1 μm membrane (Cytiva). Uniform size of the liposomes was confirmed by DLS. For liposome fusion experiments, the liposomes were diluted to 1 mM total lipid in 50 mM citrate-phosphate buffer (Boston Bioproducts) at the desired pH and subsequently mixed with a 21× volume of LNP sample at approximately 0.476 mM total lipid (estimated based

on mRNA concentrations) to final concentration of 10× relative to the liposomes. A negative control was included where liposomes were diluted with additional buffer, and a positive control with a final concentration of 0.36% Triton-X 100 (Fisher) to established F_{min} and F_{max}. Following a 30 min incubation at room temperature, samples were plated in triplicate in a 96-well plate, and fluorescence was measured on a SpectraMax M5 microplate reader (Molecular Devices, San Jose, CA). NBD fluorescence was measured with an Ex/Em of 465/520 nm, and FRET was measured with Ex/Em of 465/580 nm. F_{max} was taken as the average of the positive control wells for NBD fluorescence, and the negative control wells for the FRET measurements, and *vice versa* for F_{min}. %Lipid fusion and %FRET were calculated as $(F_{sample} - F_{min})\,(F_{max} - F_{min})^{-1} \times 100\%$.

Ultra performance liquid chromatography with charged aerosol detection (UPLC-CAD)

Separation of lipids *via* UPLC was performed on an Acquity H-Class (Waters) and CAD peaks were detected using a Corona Veo charged aerosol detector (Thermo Scientific). LNPs were dissolved in 80% isopropanol (v/v) prior to injecting 0.5 μL onto an XSelect CSH C18 column (Waters). Separation was performed at 25 °C using a stepwise gradient of 50 : 50 water : methanol with 0.1% formic acid and 50 : 50 methanol : acetonitrile with 0.1% formic acid at a flow rate of 0.6 mL min^{-1}.

Laurdan assay (lipid fluidity)

Laurdan dye (6-dodecanoyl-2-dimethylaminonaphthalene; Invitrogen) was dissolved to 0.2 mg mL^{-1} in DMSO, and further diluted to 1.44 μM in 300 mM citrate-phosphate buffer (Boston Bioproducts) at each desired pH. Separately, LNP formulations were diluted to approximately 3.12 mM total lipid with 10% trehalose. For each pH point, 157 μL of diluted Laurdan dye in buffer was pipetted into 3 replicate wells in a 96-well plate, and 43 μL of diluted LNPs were added and mixed *via* pipetting. Plates were incubated at room temperature for 3 h, after which fluorescence was measuring on a SpectraMax M5 microplate reader (Molecular Devices, San Jose, CA). Fluorescence emissions were measured from 400–600 nm in steps of 10 nm using an excitation wavelength of 340 nm. Generalized polarization (GP) values were calculated using eqn (2) (see Results section).

SAXS

SAXS measurements were performed on a Xeuss 3.0 SAXS/WAXS system (Xenocs Inc., Holyoke, MA) equipped with a Genix 3D Cu microfocus source (Cu Kα, λ = 1.5418 Å) and an Eiger 1 M detector (Dectris). Samples were loaded into the BioCube sample environment using a robotic autosampler, and measurements were conducted at 25 °C. Two-dimensional scattering data were azimuthally averaged, buffer-subtracted, and converted to one-dimensional scattering profiles using XSACT software. Samples were measured at two sample-to-detector distances: 0.55 m and 2.016 m. The data from both distances were merged to produce a single SAXS profile. All LNP formulations were stored frozen and thawed to room temperature immediately prior to analysis.

Cryo-TEM

All mRNA–LNPs were buffer-exchanged into nuclease-free water (Millipore Sigma), vitrified by plunge-freezing, and imaged using brightfield cryo-transmission electron microscope. TEM grids (Quantifoil GmbH) were glow-discharged for 25 seconds using a Pelco EasiGlow (Ted Pella). Samples were applied to grids in the chamber of a Vitrobot Mk IV system (ThermoFisher) at 95% relative humidity and 22 °C, blotted, and then plunged into liquid ethane for vitrification. Each sample was vitrified on Quantifoil R2/1200 mesh grids, both with and without a continuous carbon film of 2 nm nominal thickness. Imaging was performed either on a Talos Arctica transmission electron microscope (FEI Company) with a K2 direct electron detector (Gatan) controlled by SerialEM software at 49 000× and 130 000× nominal magnification (corresponding to pixels sizes 0.56 nm per px and 0.21 nm per px respectively), or on a Tundra transmission electron microscope (ThermoFisher) equipped with a camera controlled by EPU software at 69 000× and 110 000× nominal magnification. Images were collected from grids showing optimal ice thickness and low contamination. Regions of interest in the images displaying supramolecular structures were identified.

QCM-D characterization

Shifts in resonance frequency (ΔF) and dissipation (ΔD) for odd overtones (n = 1, 3,..., 13) were recorded using a QSense Pro (Q-Sense Inc., Gothenburg, Sweden). The data followed similar trends at all overtones measured; for clarity, only data for the fifth overtone (n = 5) is shown. Gold-coated QCM-D sensors (QSX301, Biolin Scientific) were initially subjected to UV/ozone cleaning in a UV/Ozone ProCleaner Plus (Bioforce Nanosciences) for 10 min prior to being submerged in a cleaning solution of approximately 3.6% ammonium hydroxide (Thermo Scientific) and 4.3% hydrogen peroxide (Fisher) for 5 min at 75 °C. Sensors were then rinsed gently with RNAse-free water, dried using nitrogen, and subjected to a second UV/ozone cleaning for 10 min prior to loading onto the machine sensor plate.

Each protein was deposited onto the sensors by injecting 0.1 mg mL^{-1} in pH 7.4 PBS (Fisher) at 30 μL min^{-1} for 20 min. The deposited protein was then rinsed with PBS at 40 μL min^{-1} for 10 min. LNPs were diluted in 10% trehalose to a concentration of 0.05 mg mL^{-1} total mRNA in PBS, prior to flowing over the deposited protein layers at 40 μL min^{-1} for 90 min. Sensors were subsequently rinsed with PBS. All experiments were performed at 37 °C.

Data analyses

Plots and mathematical regressions were generated in Prism 10 (GraphPad). Unpaired parametric *t*-tests with Welch's correction were used for tests of statistical significance. AF4-MALS data was analyzed using Astra 8.2 software. To analyze the particle distribution, the configuration from BSA was applied to the samples and appropriate baselines were drawn for all detectors. The appropriate start and end points for each peak

were determined based on the rms radius, hydrodynamic radius, and molar mass. Particle count was determined using the first order sphere model while particle mass, PDI ($M_w \cdot M_n^{-1}$), and shape factor were determined using a second order Debye fit. CAD traces for UPLC were analyzed using Empower 3 software (Waters) and compared to lipid standards for the calculation of molar ratios. SAXS data were plotted and analyzed using OriginPro 2024. Bragg peaks of SAXS profiles were deconvoluted using Origin's built-in "Peak deconvolution" app. After establishing a baseline, the peaks were fitted with a Lorentz function to obtain the peak position, height, FWHM, and area. Raw QCM-D data was analyzed in Dfind (Biolin Scientific). Fast Fourier transform (FFT) and periodicity measurements of Cryo-TEM images were conducted using the 1.53c Fiji distribution of ImageJ.[34] Figures were made in part using Biorender (https://www.biorender.com).

Results and discussion

Fig. 1 presents a schematic of the formulation process employed, with the variables highlighted in red. To formulate the LNPs, hEPO mRNA in acidic buffer was T-mixed with a lipid mixture in ethanol at different flow rates using T's of varying diameters to generate different degrees of turbulence (Re) in the mixing chamber. The starting investigation focused on changes in Re, while all other parameters, like the lipid : mRNA mass ratio, molar ratios of lipids, and flow rate ratio (FRR), were kept constant.

Increased Re increases hEPO expression *in vivo*

The effects of Re on particle size, mRNA encapsulation efficiency, and *in vivo* protein expression of LNPs made with OF-02 are shown in Fig. 2. Particle size (hydrodynamic diameter measured by DLS) decreased with increasing Re consistently across the laminar mixing region; however, there were minimal changes to LNP size at/above Re values in the transitional region (Fig. 2A, left). Characterization of OF-02 LNPs by AF4-MALS-dRI-UV-DLS corroborated the DLS data, showing that particles were generally best described as uniform spheres with decreasing particle mass at higher Re (Fig. S1A). Measurements of polydispersity index (PDI) and estimates of particle counts per RNA mass for spherical particles by AF4-MALS-dRI-UV-DLS indicated no particular trends with Re (Fig. S1B). There were spikes in both PDI and normalized particle count at Re values of 937 and 4686; however, the lack of any apparent trend with Re suggests that these differences may not be related to changes in the mixing process. Encapsulation of mRNA, as measured by Ribogreen assay, increased sharply from the lowest Re (Re = 234) to the second-lowest (Re = 937), but there were minimal changes with more turbulent mixing (Fig. 2A, right). Similar trends were observed for hEPO-LNPs formulated with 2 other structurally different proprietary ionizable lipids (data not shown).

Changes in hEPO protein expression as a function of Re are shown in Fig. 2B. Briefly, mice were injected with OF-02 LNPs encapsulating hEPO mRNA *via* I.M. (gastrocnemius muscle) or I.V. (tail vein) routes of administration, and blood was collected after 6 h (I.M.) or 24 h (I.V.) and analyzed by ELISA. In each individual study, 4 mice/group were injected with equal mRNA doses of LNPs at each Re and expression was normalized to the average hEPO expression for the cohort injected with the lowest-Re (234) LNPs; data from multiple studies is shown. For both injection routes, statistically significant increases in expression were observed between the groups injected with the lowest and highest Re-LNPs. Slightly different results were

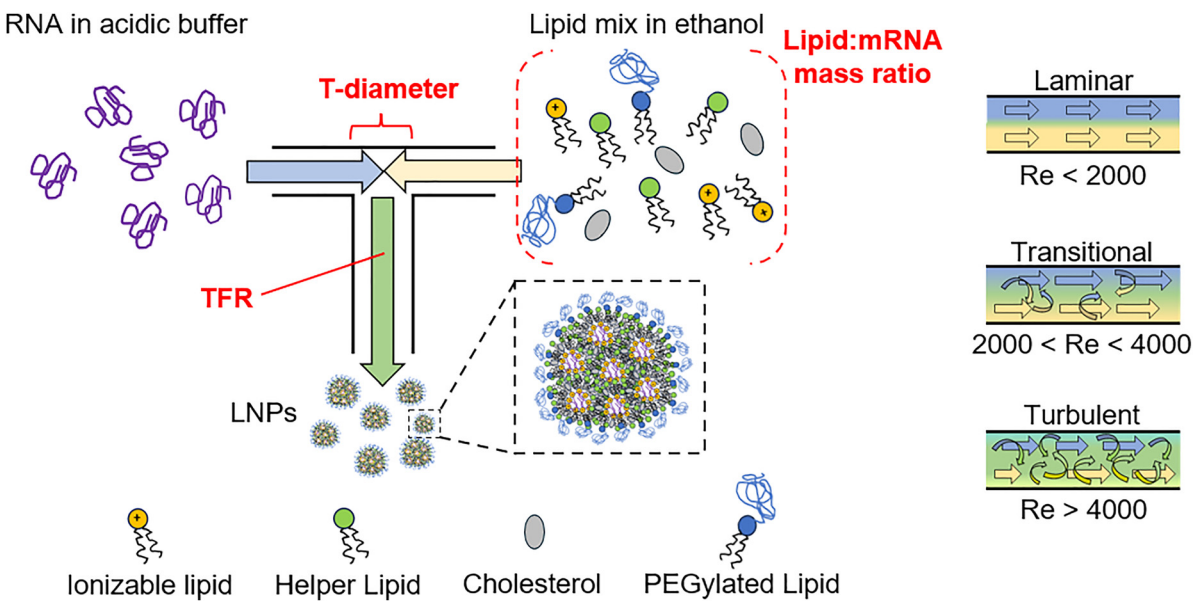

Fig. 1 Overall experimental design for this study. mRNA–LNPs were prepared from the same general lipid composition *via* T-mixing, while variables are highlighted in red bold. The key metric of Re is illustrated and general ranges for laminar, transitional, and turbulent mixing are defined.

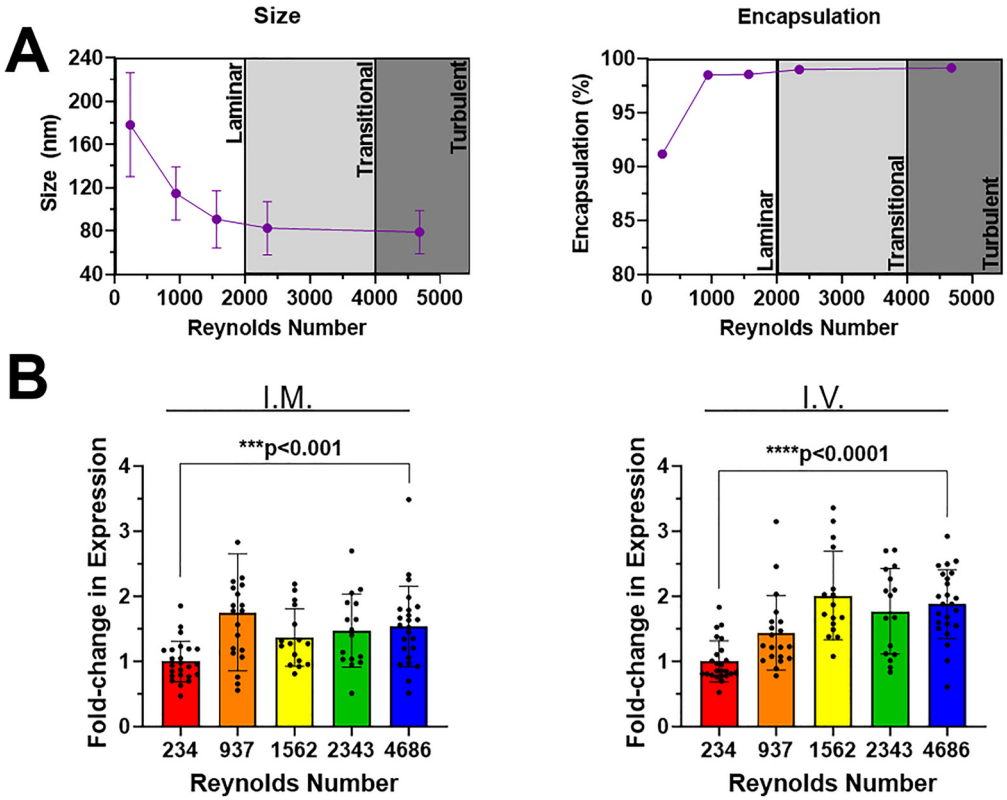

Fig. 2 General characterization and *in vivo* hEPO expression for OF-02 LNPs with regard to Re. (A) Size decreases to a minimum and encapsulation increases to a maximum with increasing Re. (B) *In vivo* expression of hEPO *via* two injection routes for LNPs made at different Re. Expression generally increases with increasing Re, with statistically significant increases for either route of administration between the lowest and highest Re tested.

observed for I.M. *versus* I.V. administration: hEPO expression *via* I.V. injection increased with increasing Re up to the "transitional" mixing domain and was relatively unchanged thereafter, whereas for I.M. administration, expression consistently increased with Re with the exception of Re = 937, where there was an unexpected spike. The differences between expression for LNPs made at the higher end of Re range were less statistically significant, making it challenging to conclude confidently that there is any benefit from additional turbulence beyond the "transitional" region. In spite of this, increased Re generally resulted in increased expression up to a maximum approaching 2-fold for the I.V. route of administration and approximately 50% *via* I.M. injection for this particular mRNA–LNP system.

Increased Re promotes fusion with endosomal membrane mimic model vesicles at early endosomal pH

In light of the *in vivo* results, we hypothesized that LNPs made at higher Re could display greater endosomal fusion, increasing intracellular release of mRNA. To test this hypothesis, we employed an *in vitro* fusion assay using model endosomes. In short, anionic vesicles were prepared *via* thin film rehydration of a 48 : 25 : 25 : 1 : 1 mol% mixture of DOPE, DOPC, DOPS, NBD-PE, and Liss Rhod-PE, respectively, and incubated with all the mRNA–LNPs at pH ranging from 3.5 to 7.5. Fusion between LNPs and model endosomes was then measured by monitoring fluorescence emission from the NBD fluorophore or decreased Förster resonance energy transfer (FRET) intensity between the NBD donor fluorophore and Liss-rhodamine acceptor as the fluorescently labeled lipids within the vesicles were diluted upon fusion with the LNPs.

The results of the liposome fusion assay are shown in Fig. 3. Upon incubation of model endosomes with LNPs, an increase in %lipid fusion, as a measure of NBD fluorescence, was observed for all LNPs at all pH tested. Very little fusion ($<10\%$) was observed at pH 7.5 for LNPs made at any Re, likely because the ionizable lipid is expected to be mostly deprotonated at this pH. However, there was greater fusion at early endosomal pH 6.5 and 5.5, modeled well with an exponential curve ("one-phase association" in GraphPad Prism 10) at pH 6.5, with lipid fusion increasing most at the lower end of the Re range. This relationship between the apparent fusogenicity of LNPs and higher Re suggests the possibility of distinct structural features in these LNPs that help facilitate membrane fusion, escape, and release of the mRNA cargo in acidifying endosomes. Interestingly, however, the trend between Re and fusogenicity appeared to dissipate as pH decreased further: there was no apparent dependence of fusogenicity on Re at pH 4.5 (although the magnitude was just as great as pH 5.5–6.5), and there was a trend toward lower lipid fusion with higher Re at pH 3.5. This may reflect an inherent limitation of the assay at low pH, as the fluorescence intensity of NBD derivatives has been shown to depend on pH and microenvironment polarity.[35–38] When assaying FRET intensity, in which decreased FRET

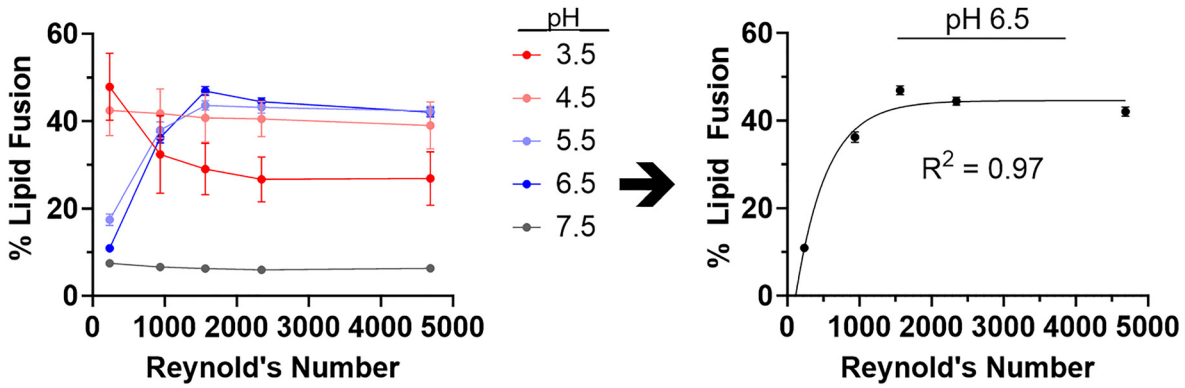

Fig. 3 Liposome fusion results from FRET assay. %Lipid fusion typically increases with increasing Re at pH < 7.5, with the greatest differences observed at pH 5.5 and 6.5. Exponential fit shows good correlation between %lipid fusion and Re at pH 6.5.

indicates greater fusion, the trend of lower FRET intensity with higher Re held true at pH 4.5 and 3.5; however, the magnitude of fusion was apparently reduced – potentially again due to decreased NBD emission intensity (Fig. S2). Notwithstanding this limitation of the assay, the data indicate that OF-02 LNPs made at higher Re are more fusogenic in the pH range most relevant for endosomal escape.[39–41]

LNP biophysical characteristics support mechanistic model for increased fusogenicity at increased Re

In light of the observed boost in hEPO expression and increased fusogenicity at endosomal pH of LNPs made at higher Re, we next sought to gain a mechanistic understanding of the underlying biophysical characteristics of these LNPs. Zeta potential was measured across a range of physiologically relevant pH as described in Materials & Methods to evaluate the effects of varying Re on the electrostatic properties of the LNPs in an *in vivo* environment.[42] Similar overall trends were observed for LNPs made at each Re (Fig. 4A); each curve was well-fit by a third-order polynomial, and zeta potential decreased from about +20 mV at pH 3.5 to around −5 mV at pH 7.5. However, a clear pattern emerged at pH 4.5, wherein LNPs formulated at lower Re had higher zeta potential than those formulated under more turbulent mixing conditions. The magnitude of this change was

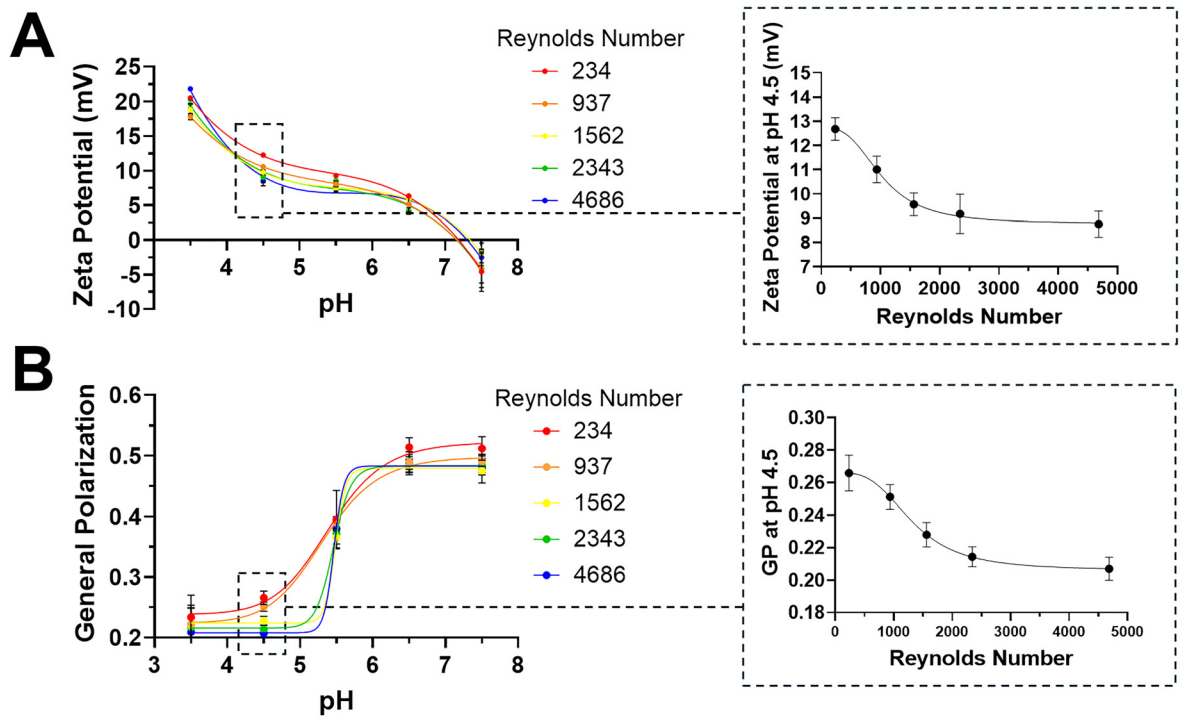

Fig. 4 Biophysical characteristics of OF-02 LNPs supporting a mechanistic model of how Re affects *in vivo* expression. (A) Zeta potential *versus* pH for OF-02 LNPs formulated at different Re. Zeta potential decreases with increasing pH for all LNPs, however LNPs made at higher Re have lower zeta potentials at pH 4.5. (B) General polarization (GP), as measured by Laurdan assay, as a function of pH for OF-02 LNPs prepared at different Re. GP increases with pH for all formulations, however LNPs made at higher Re have lower GP at pH 4.5.

greatest between the three lowest-Re formulations, consistent with the trends observed for size, encapsulation, and fusogenicity. Analyzing the shapes of the zeta potential curves, the coefficients of the terms in the polynomial fits were typically higher for LNPs formulated at higher Re (Table S2), leading to greater changes in zeta potential at the extreme ends of the curve and relatively little change around endosomal pH ranges. Based on these results, we hypothesized that a greater proportion of the ionizable lipid is likely "buried" in the hydrophobic core of the higher-Re LNPs, owing to more-complete mixing and closer association with the mRNA cargo. Importantly, the differences in zeta potential did not appear to be caused by different total amounts of ionizable lipid in the LNPs, as lipid quantification and analysis by UPLC-CAD did not reveal any noteworthy differences in the molar ratio of OF-02 or the total lipid content per mRNA mass in correlation with Re (Fig. S3). Regarding differences in mRNA encapsulation between the samples, lower encapsulation (more free mRNA) would be expected to result in lower zeta potential if mRNA was bound to the positively charged nanoparticles; however, we see the opposite trend. Based on these results, we speculated that the differential presumed partitioning of the ionizable lipid may give rise to different structural features in acidifying endosomes for LNPs formulated at higher Re, which could facilitate membrane fusion and cytosolic release of mRNA cargo. This model would be consistent with the relative lack of change in zeta potential for LNPs made at higher Re between pH 6.5 and 4.5 and the results of the liposome fusion assay, as well as previous reports highlighting the importance of pH-driven structural transitions in RNA delivery.[39,41,43,44]

$$\mathrm{GP} = \frac{I_{440} - I_{490}}{I_{440} + I_{490}} \quad (2)$$

Eqn (2). Calculation of GP for the Laurdan assay, where I_{440} is the fluorescent intensity at 440 nm and I_{490} is the intensity at 490 nm.

To test the hypothesis about pH-driven structural rearrangements, we measured the lipid fluidity and membrane packing of the LNPs as a function of pH using Laurdan Assay. Laurdan reagent is a lipophilic fluorophore that partitions into LNPs in aqueous solution, causing a shift in fluorescence emission toward shorter wavelengths in environments with greater lipid packing. The degree of this shift can be quantified by calculating a "general polarization" (GP) value (eqn (2)), with lower GP values indicating more lipid fluidity. As shown in Fig. 4B, reading the graph from right to left, GP decreased for all LNPs with decreasing pH, indicating a greater degree of lipid fluidity in acidic environments. Other groups have also demonstrated a positive relationship between increased lipid fluidity as measured by Laurdan assay and *in vivo* expression, presumably resulting from greater fusability of less densely-packed LNPs.[44,45] While trends in GP were broadly similar for LNPs made at different Re, LNPs formulated at higher Re had lower GP at pH 4.5 than those formulated at lower Re – a trend that closely mirrored that which we observed for zeta potential. In fact, GP values were generally lower for LNPs formulated at higher Re at all pH tested, although the differences were greatest at pH 4.5 (Fig. S4). Once again, the magnitude of change in this biophysical attribute was greatest when comparing laminar to transitional Re values, but was relatively small comparing the two highest Re formulations. Upon generating sigmoidal fits of the curves of GP *vs.* pH, it appears that the difference in GP between high/low-Re samples is maximized around pH 5.0, owing to the greater slopes of the curves in the endosomal pH range. Taken together, these results indicate that more turbulent mixing produces LNPs that undergo a more dramatic change in lipid fluidity around endosomal pH, resulting in overall increased lipid fluidity at pH 4.5, potentially resulting from a greater percentage of ionizable lipid in the LNP core. Although the trend between GP and Re was not as pronounced at pH 5.5 or 6.5, the change in lipid fluidity as a function of pH suggests that different structural changes for LNPs made at different Re may be partially responsible for the greater fusogenicity of these particles at endosomal pH.

To further investigate the effects of Re on LNP internal structure, LNPs were analyzed using small-angle X-ray scattering (SAXS) at varying pH (Fig. 5). Two main peaks were identified: "peak 1" centered around $q \sim 0.12$–0.13 Å^{-1}, and "peak 2" at $q \sim 0.15$ Å^{-1}. Peak 1 has a d-spacing of ~4.8–5.2 nm, whereas peak 2 has a d-spacing of ~4.2 nm, indicating two distinct structures—most likely inverse hexagonal and multilamellar phases, respectively, as supported by cryo-TEM image analysis discussed below. Representative SAXS profiles over the full q-range are provided in Fig. S5. Guinier analysis in the low-q region (Table S3) shows that the radius of gyration (R_g) ranges from 26 to 75 nm, correlating well with the increase in hydrodynamic radius (R_h) from 40 to 92 nm as Re decreases. Fig. 5A compares the SAXS patterns for the lowest- and highest-Re LNPs as a function of pH. At pH 6.5–7.5, peak 1 predominated, however the higher-q peak 2, corresponding to a denser structure, became more evident at pH 5.5. At pH 4.5, the average q-value for both LNPs shifted lower, possibly indicating an overall swelling of the LNP structure as the ionizable lipid becomes fully protonated; however, the relative contribution of the denser peak 2 structure was notably more prominent for the low-Re LNPs. To further illustrate the effects of Re in this pH range, the SAXS profiles for LNPs formulated at all Re tested were compared in Fig. 5B. At pH 5.5, there was an apparent contribution from both peak 1 and peak 2 substructures at all Re, but the resolution of these peaks decreased with increasing Re, indicating less heterogeneity in the LNP structure. At pH 4.5, the two peaks became even less well-resolved for LNPs at every Re, as the structures began to converge.

To quantify the relative contributions of the structures indicated in the SAXS patterns, OriginPro 2024 was used to deconvolute the peaks and estimate their relative intensity (Fig. 5C). As pH decreased from 7.5 to 4.5, there was an overall increase in the total area of the peaks for LNPs at all Re, indicating a common feature of more ordered structure with decreasing pH. The lower-q structure corresponding to peak 1 predominated across all Re at pH 7.5 and 6.5, while peak 2 became more prominent at pH 5.5 and 4.5. The relative

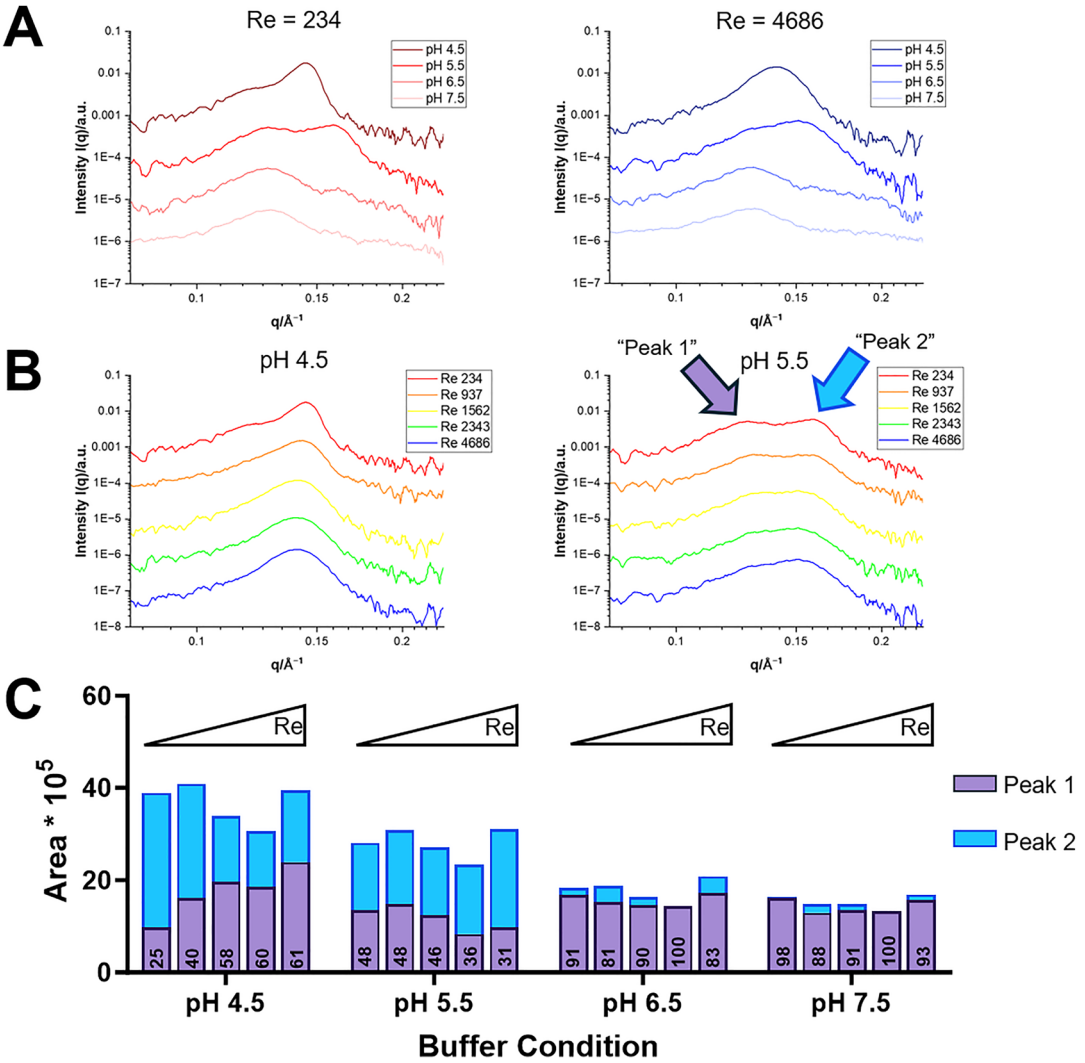

Fig. 5 SAXS pattern of LNPs made at different Re. (A) pH dependence of SAXS pattern of LNPs formulated at the lowest (left) and highest (right) Re. With decreasing pH, overall signal intensity increases and distinct distributions of peaks between the two samples become more apparent. (B) Comparison of SAXS profiles at pH 4.5 (left) and pH 5.5 (right) for all LNP samples. Lower Re results in greater separation of peaks. (C) Peak area integrations from deconvoluted SAXS patterns comparing all Re across a range of pH. Total peak area increases with decreasing pH, and the relative contribution of peak 1 increases with increased Re at pH 4.5. Peak 1 area as percent of total is provided over the purple bars.

contribution of this higher density structure was comparable across Re at pH 5.5; however, upon further reduction of pH to 4.5, there was a clear trend between peak 1 area and increased Re. For LNPs made at the lowest-Re, peak 1 comprised only 25% of the total peak area, increasing to 40% at Re = 937, and again to 58% at Re = 1562, and was relatively unchanged thereafter at the two highest Re values. Corroborating morphological analyses by Cryo-TEM showed that there is more heterogeneity in the types of structures present in the lowest-Re sample (Fig. S6A), whereas LNPs made at the highest Re are more uniform (mostly compact cores with negligible liposomes or blebs) and have considerable inverse-hexagonal structures (Fig. S6B), the likes of which have been correlated with endosomal escape efficiency previously.[46,47] Fast Fourier Transforms (FFTs) of the images revealed different diffraction patterns between the lowest- and highest-Re samples, suggesting differences in periodicity between the hexagonal structures present in the LNPs. Hexagonal lipid structures exhibited periodicities in the range of 3–4 nm, with differences observed between low-Re (Re = 234) and high-Re (Re = 4686) formulations. These polymorphic variations likely reflect genuine differences in lipid self-assembly driven by mixing conditions and are less likely to be due to cryo-preparation artefacts, given the supporting orthogonal analytical observations from SAXS, *etc.* The differences in diffraction patterns may be expected to affect the behavior of these particles in biological systems or upon storage; the greater structural homogeneity of high-Re LNPs, *i.e.* ~100% compact cores *vs.* ~80%, suggests potentially more predictable stability characteristics. The relative abundance of "peak 1" in the SAXS profiles increased significantly in higher Re LNPs at pH 4.5, indicating a structural transition consistent with the morphological differences observed in Cryo-TEM

images. This structural reorganization may correlate with enhanced protein expression *in vivo*, though the mechanistic basis of this relationship warrants further investigation.

LNPs made at higher Re have increased serum protein binding

Moving beyond LNP biophysical attributes that may contribute to intracellular release of mRNA, we next turned our attention to extracellular factors like serum protein binding. It is well-appreciated that binding of key serum proteins by mRNA–LNPs is a critical factor affecting uptake and tissue-specific expression *via* receptor-mediated transport.[48] Moreover, our *in vivo* studies demonstrate that hEPO expression was typically higher per mass of mRNA injected for I.V. administration (Fig. S7). Hence, we evaluated the binding affinity of three serum proteins involved in receptor-mediated uptake, namely apolipoprotein E3 (Apo-E3), apolipoprotein A1 (Apo-A1), and albumin, to OF-02 LNPs formulated at different Re by Quartz crystal microbalance with dissipation (QCM-D). In turn, each protein was immobilized on a gold sensor plate, over which LNPs were flowed and changes in resonance frequency were collected to quantify binding. In line with the observed increases in expression, we noted greater protein binding to LNPs made at higher Re for all three serum proteins tested (Fig. 6). The effect was most pronounced when comparing higher-Re formulations to the lowest-Re sample, with the two highest-Re formulations showing comparable binding of each protein. Between the three proteins, we observed the greatest absolute change in frequency for binding of Apo-E3, consistent with its important role in LNP transport following systemic administration.[32] We also noted an interesting trend for binding of Apo-A1: all LNPs appear to bind this protein rapidly at first, however there is a second, slower binding phase for the two highest-Re LNPs, which may reflect alternative binding modes. It is possible that increased surface area to volume ratio of the smaller particles and more numerous and uniform nanoparticles formulated at higher Re *versus* the lowest Re could partially account for the greater degree of binding we observed, although particle counts by AF4-MALS did not strictly trend with the intermediate Re

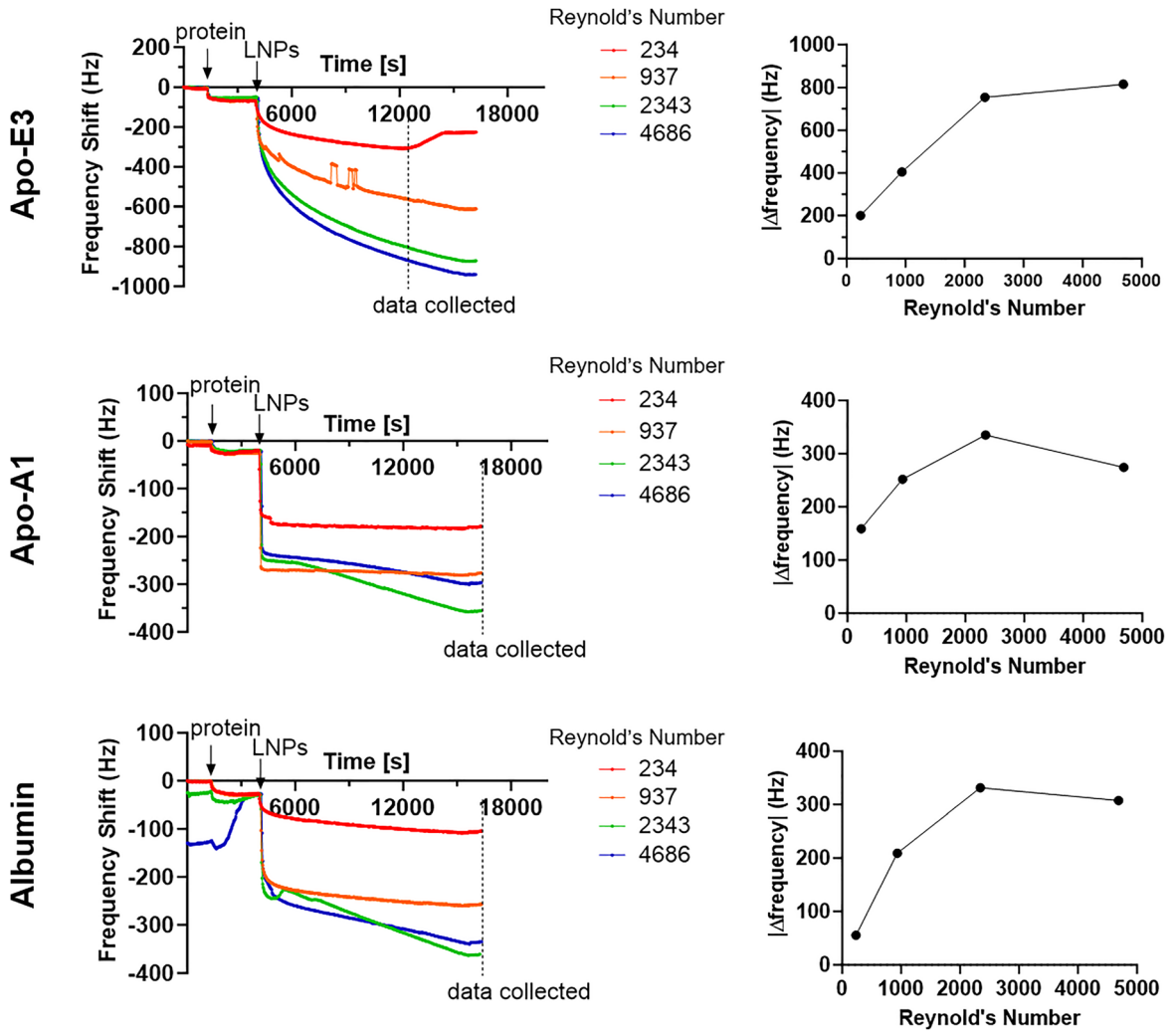

Fig. 6 *In vitro* serum protein binding of OF-02 LNPs made at different Re, as measured by QCM-D. Protein binding, as measured by changes in frequency, is greater for LNPs made at higher Re for human Apo-E3, Apo-A1, and albumin.

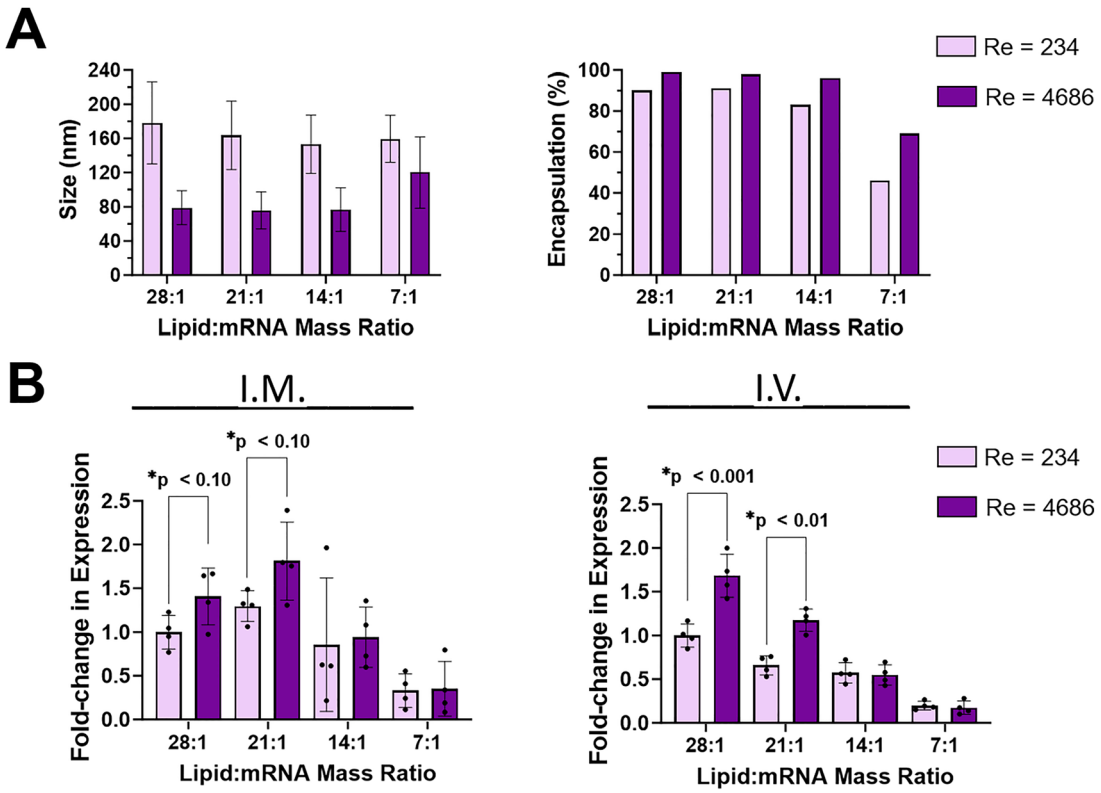

Fig. 7 General characterization and *in vivo* hEPO expression of OF-02 LNPs made at different lipid : mRNA mass ratios under laminar *vs.* turbulent mixing conditions. (A) Particle size decreases and encapsulation efficiency increases with turbulent mixing conditions. (B) *In vivo* hEPO expression *via* two injection routes. Statistically significant increases in expression are observed for LNPs at 28 : 1 and 21 : 1 lipid : mRNA mass ratios at higher Re, while the differences are not significant at lower mass ratios.

(Fig. S1). Nevertheless, with increased binding of all three proteins with LNPs made at higher Re, we infer that increased Re during the formulation process may boost *in vivo* expression by increasing uptake of LNPs bound to serum proteins involved in receptor-mediated transport, in addition to the aforementioned mechanisms involving intracellular mRNA release.

Higher Re increases hEPO expression of LNPs made at different lipid : mRNA mass ratios

Having demonstrated that higher Re can be employed to improve the potency of mRNA–LNPs, we asked whether this phenomenon could be leveraged to increase *in vivo* expression of LNPs made at reduced lipid : mRNA mass ratio, which is often a key factor in LNP optimization.[18] LNP components – especially the ionizable lipid – can pose concerns regarding tolerability and reactogenicity,[49] so strategies to reduce lipid load per dose of mRNA would be of significant merit towards developing LNP-based vaccines and therapies. To this end, we formulated OF-02 LNPs encapsulating hEPO mRNA at four different lipid : mRNA mass ratios, varying from 28 : 1 down to 7 : 1, comparing our highest and lowest Re used in this study. As before, we observed decreased particle size and increased mRNA encapsulation efficiency for the high-Re condition at all the ratios tested (Fig. 7A). Notably, LNPs made with a mass ratio of 7 : 1 (7 mg total lipid per 1 mg mRNA) had lower encapsulation overall, potentially because there is insufficient ionizable lipid to fully self-assemble with the mRNA and incorporate it into the LNP core; however, encapsulation was still in an acceptable range for lipid : mRNA mass ratios of 14 : 1 and above. We next tested each combination of Re and lipid : mRNA mass ratio for *in vivo* expression *via* I.M. and I.V. administration (Fig. 7B). We observed statistically significant increases in expression between the two Re LNPs for mass ratios of 28 : 1 and 21 : 1 *via* both I.M. and I.V. injections; no such boost was observed for mass ratios of 14 : 1 or 7 : 1. However, expression of the high-Re formulation at a mass ratio of 21 : 1 was greater than that of the low-Re 28 : 1 condition, though the statistical significance was low with the small cohort size (p = 0.10). Nonetheless, these results indicate that employing higher Re could be used to boost protein expression for LNPs made at reduced lipid : mRNA mass ratios, to possibly alleviate lipid-mediated reactogenicity without compromising LNP function.

Conclusions

Herein, we present data supporting a mechanistic model by which formulating OF-02 LNPs at higher turbulence T-mixing (higher Re) improves *in vivo* protein expression. From measurements of zeta potential and lipid packing *via* the Laurdan assay across a physiologically-relevant pH range, we hypothesize that higher Re likely promotes faster and uniform mixing of OF-02 LNPs, leading to consistent supersaturation and nucleation

rate of the LNP components, with perhaps a greater proportion of ionizable lipid partitioned into the LNP core, leading to a more dramatic shift in lipid fluidity at endosomal pH, and consequently improved mRNA release from acidifying endosomes in cells. This hypothesis is further supported by the *in vitro* liposome fusion assay, which showed that LNPs made at higher Re are more fusogenic, particularly at pH 5.5 and 6.5. Direct observation of pH-dependent structural features by SAXS confirms that LNPs made at different Re have distinct structural profiles that may contribute to their differential performance *in vivo*.

Beyond LNP features that may affect endosomal escape and intracellular mRNA release, results from QCM-D experiments show that LNPs made at higher Re have higher serum protein binding. This observation suggests that greater receptor-mediated uptake may also play a role in increased protein expression for LNPs made at higher Re, especially *via* intravenous administration. Lastly, a brief study examining the effects of Re at reduced lipid : mRNA mass ratios suggests that more turbulent mixing may be used in some scenarios to reduce lipid load while maintaining similar levels of protein expression. In the future, direct observation of increased endosomal escape in cultured cells and/or measurements of LNP uptake *in vivo* would help confirm this proposed model of the effects of Re on LNP performance. The effects of Re on LNPs with different lipid components, lipid compositions, and cargos also remains to be evaluated. The authors acknowledge the limitations of the current data set, whose scope does not cover the full design space of pipe diameter and fluid velocity combinations; it would thus be worthwhile to conduct similar experiments at scale using a standardized T-mixer size and faster flow rates to examine the relevance of these findings to LNP commercialization. Nevertheless, this work constitutes a critical step in connecting the effects of mixing chamber turbulence on LNP biophysical attributes to protein expression *in vivo.*

Author contributions

The manuscript was written through contributions of all authors. All authors have given approval to the final version of the manuscript. Richard Mosesso: study design, LNP formulation, analytical characterization, data analysis, coordination with collaborators, manuscript drafting and figure preparation; Katie Randall: LNP formulation and contextualization of results with prior literature; Amita Vaidya: project management, experimental design and strategy, coordination with collaborators, manuscript and figure review and preparation; Jackie Tang: sample submission and data analysis for SAXS studies; Trent Northen: AF4-MALS method optimization, data acquisition, and analysis; Aurélie Deliot: cryo-TEM image analysis and figure preparation; Mengwei Sun: assistance with QCM-D data acquisition and analysis; Rebecca Goldman: early proof of concepts and experimental design; Adam Lyons: zeta potential measurements, Lingyun Liu: sample submission and coordination, method development, and data analysis for SAXS studies; Shrirang Karve: supervision, manuscript and figure review and preparation; Frank DeRosa: manuscript and figure review and preparation.

Conflicts of interest

The authors declare the following financial interests/personal relationships which may be considered as potential competing interests: all the authors are current employees of Sanofi and may hold stock of the company.

Data availability

All data supporting this article have been included as part of the supplementary information (SI). Supplementary information: Supplemental Table 1. Calculations of Re for T-mixers and flow rates. Supplemental Fig. 1. Characterization of OF-02 LNPs by AF4-MALS-dRI-UV-DLS. Supplemental Table 2. Coefficients and R^2 values for trinomial fits of zeta potential measurements as a function of pH. Supplemental Fig. 2. Analysis of model endosome fusion with LNPs made at different Re by FRET. Supplemental Fig. 3. UPLC-CAD analysis of OF-02 LNPs made at different Re. Supplemental Fig. 4. Comparisons of general polarization *via* Laurdan assay at different pH. Supplemental Fig. 5. Representative SAXS profiles in 10% trehalose for OF-02 LNPs made at different Re. Supplemental Table 3. Differences in hydrodynamic radius (R_h) and radius of gyration (R_g) *versus* Re. Supplemental Fig. 6. Cryo-TEM images reveal distinct populations of particles in LNPs made at high *versus* low Re. Supplemental Fig. 7. Comparison of I.M. and I.V. routes of administration for OF-02 LNPs. See DOI: https://doi.org/10.1039/d6tb00052e.

Acknowledgements

The research included in the manuscript was funded by Sanofi. The authors would like to thank Dr Barak Yahalom at Alpha Preclinical for managing all *in vivo* studies. We would also like to thank Dr Ashley Bernstein and Prof. Jason Kaelber from the RCNF at Rutgers university for acquisition of the Cryo-TEM images. We also thank Josue San Emeterio and Scott Barton at XENOCs for the SAXS data acquisition and analysis. We thank Dipen Parande and Saket Dolare at Sanofi for guidance and training on the UPLC-CAD and liposome fusion assay, respectively.

References

1 D. Adams, A. Gonzalez-Duarte, W. D. O'Riordan, C.-C. Yang, M. Ueda, A. V. Kristen, I. Tournev, H. H. Schmidt, T. Coelho, J. L. Berk, K.-P. Lin, G. Vita, S. Attarian, V. Planté-Bordeneuve, M. M. Mezei, J. M. Campistol, J. Buades, T. H. B. III, B. J. Kim, J. Oh, Y. Parman, Y. Sekijima, P. N. Hawkins, S. D. Solomon, M. Polydefkis, P. J. Dyck, P. J. Gandhi, S. Goyal, J. Chen, A. L. Strahs, S. V. Nochur,

M. T. Sweetser, P. P. Garg, A. K. Vaishnaw, J. A. Gollob and O. B. Suhr, *N. Engl. J. Med.*, 2018, **379**, 11–21.
2 F. P. Polack, S. J. Thomas, N. Kitchin, J. Absalon, A. Gurtman, S. Lockhart, J. L. Perez, G. P. Marc, E. D. Moreira, C. Zerbini, R. Bailey, K. A. Swanson, S. Roychoudhury, K. Koury, P. Li, W. V. Kalina, D. Cooper, R. W. Frenck, L. L. Hammitt, Ö. Türeci, H. Nell, A. Schaefer, S. Ünal, D. B. Tresnan, S. Mather, P. R. Dormitzer, U. Şahin, K. U. Jansen, W. C. Gruber and C. C. T. Group, *N. Engl. J. Med.*, 2020, **383**, 2603–2615.
3 L. R. Baden, H. M. E. Sahly, B. Essink, K. Kotloff, S. Frey, R. Novak, D. Diemert, S. A. Spector, N. Rouphael, C. B. Creech, J. McGettigan, S. Khetan, N. Segall, J. Solis, A. Brosz, C. Fierro, H. Schwartz, K. Neuzil, L. Corey, P. Gilbert, H. Janes, D. Follmann, M. Marovich, J. Mascola, L. Polakowski, J. Ledgerwood, B. S. Graham, H. Bennett, R. Pajon, C. Knightly, B. Leav, W. Deng, H. Zhou, S. Han, M. Ivarsson, J. Miller, T. Zaks and C. S. Group, *N. Engl. J. Med.*, 2020, **384**, 403–416.
4 S. J. Thomas, E. D. Moreira, N. Kitchin, J. Absalon, A. Gurtman, S. Lockhart, J. L. Perez, G. P. Marc, F. P. Polack, C. Zerbini, R. Bailey, K. A. Swanson, X. Xu, S. Roychoudhury, K. Koury, S. Bouguermouh, W. V. Kalina, D. Cooper, R. W. Frenck, L. L. Hammitt, Ö. Türeci, H. Nell, A. Schaefer, S. Ünal, Q. Yang, P. Liberator, D. B. Tresnan, S. Mather, P. R. Dormitzer, U. Şahin, W. C. Gruber, K. U. Jansen and C. C. T. Group, *N. Engl. J. Med.*, 2021, **385**, 1761–1773.
5 X. Hou, T. Zaks, R. Langer and Y. Dong, *Nat. Rev. Mater.*, 2021, **6**, 1078–1094.
6 P. R. Cullis and M. J. Hope, *Mol. Ther.*, 2017, **25**, 1467–1475.
7 E. Samaridou, J. Heyes and P. Lutwyche, *Adv. Drug Delivery Rev.*, 2020, **154**, 37–63.
8 P. E. Saw and E. Song, *Cell Rep. Med.*, 2024, **5**, 101555.
9 Y. Zhu, L. Zhu, X. Wang and H. Jin, *Cell Death Dis.*, 2022, **13**, 644.
10 S. Xu, Z. Hu, F. Song, Y. Xu and X. Han, *Mol. Ther. Methods Clin. Dev.*, 2025, **33**, 101463.
11 Q. Cheng, T. Wei, L. Farbiak, L. T. Johnson, S. A. Dilliard and D. J. Siegwart, *Nat. Nanotechnol.*, 2020, **15**, 313–320.
12 P.-S. Wei, N. Thota, G. John, E. Chang, S. Lee, Y. Wang, Z. Ma, Y.-H. Tsai and K.-C. Mei, *J. Controlled Release*, 2024, **375**, 366–388.
13 K. Su, L. Shi, T. Sheng, X. Yan, L. Lin, C. Meng, S. Wu, Y. Chen, Y. Zhang, C. Wang, Z. Wang, J. Qiu, J. Zhao, T. Xu, Y. Ping, Z. Gu and S. Liu, *Nat. Commun.*, 2024, **15**, 5659.
14 J. A. Kulkarni, M. M. Darjuan, J. E. Mercer, S. Chen, R. van der Meel, J. L. Thewalt, Y. Y. C. Tam and P. R. Cullis, *ACS Nano*, 2018, **12**, 4787–4795.
15 S. Wang, B. Guo, H. Wang and F. Yang, *J. Drug Delivery Sci. Technol.*, 2024, **95**, 105547.
16 L. Gurba-Bryśkiewicz, W. Maruszak, D. A. Smuga, K. Dubiel and M. Wieczorek, *Biomedicines*, 2023, **11**, 2752.
17 K. Nag, Md. E. H. Sarker, S. Kumar, H. Khan, S. Chakraborty, Md. J. Islam, J. C. Baray, M. R. Khan, A. Mahmud, U. Barman, E. H. Bhuiya, M. Mohiuddin and N. Sultana, *Sci. Rep.*, 2022, **12**, 9394.
18 Md. A. Haque, A. Shrestha, C. M. Mikelis and G. Mattheolabakis, *Int. J. Pharm.: X*, 2024, **8**, 100283.
19 L. Hourdel, N. Lebaz, F. Peral, M. Ripoll, S. Briançon, F. Bensaid, S. Luthra and C. Cogné, *Int. J. Pharm.*, 2025, **672**, 125297.
20 M. Maeki, S. Uno, A. Niwa, Y. Okada and M. Tokeshi, *J. Controlled Release*, 2022, **344**, 80–96.
21 M. Maeki, Y. Fujishima, Y. Sato, T. Yasui, N. Kaji, A. Ishida, H. Tani, Y. Baba, H. Harashima and M. Tokeshi, *PLoS One*, 2017, **12**, e0187962.
22 A. Agha, W. Waheed, I. Stiharu, V. Nerguizian, G. Destgeer, E. Abu-Nada and A. Alazzam, *Discovery Nano*, 2023, **18**, 18.
23 B. G. Carvalho, B. T. Ceccato, M. Michelon, S. W. Han and L. G. de la Torre, *Pharmaceutics*, 2022, **14**, 141.
24 M. N. O. Laramy, A. P. Costa, Y. M. Cebrero, J. Joseph, A. Sarode, N. Zang, L. J. Kim, K. Hofmann, S. Wang, A. Goyon, S. G. Koenig, M. Hammel and G. L. Hura, *Mol. Pharm.*, 2023, **20**, 4285–4296.
25 Z. He, Y. Hu, T. Nie, H. Tang, J. Zhu, K. Chen, L. Liu, K. W. Leong, Y. Chen and H.-Q. Mao, *Acta Biomater.*, 2018, **81**, 195–207.
26 M. J. W. Evers, J. A. Kulkarni, R. van der Meel, P. R. Cullis, P. Vader and R. M. Schiffelers, *Small Methods*, 2018, **2**(9), 1700375.
27 S. Karve, F. DeRosa, Z. Bhavsar and M. Heartlein, Process of Preparing mRNA-Loaded Lipid Nanoparticles, US20180153822A1, *USPTO*, 2018.
28 M. Saldana, S. Gallegos, E. Gálvez, J. Castillo, E. Salinas-Rodríguez, E. Cerecedo-Sáenz, J. Hernández-Ávila, A. Navarra and N. Toro, *Fluids*, 2024, **9**, 299.
29 S. Shin, C. Devos, A. P. Udepurkar, P. K. Inguva, A. S. Myerson and R. D. Braatz, *Chem. Eng. J.*, 2025, **523**, 167786.
30 S. Chatterjee, E. Kon, P. Sharma and D. Peer, *Proc. Natl. Acad. Sci. U. S. A.*, 2024, **121**, e2307800120.
31 O. S. Fenton, K. J. Kauffman, R. L. McClellan, E. A. Appel, J. R. Dorkin, M. W. Tibbitt, M. W. Heartlein, F. DeRosa, R. Langer and D. G. Anderson, *Adv. Mater.*, 2016, **28**, 2939–2943.
32 F. Sebastiani, M. Y. Arteta, M. Lerche, L. Porcar, C. Lang, R. A. Bragg, C. S. Elmore, V. R. Krishnamurthy, R. A. Russell, T. Darwish, H. Pichler, S. Waldie, M. Moulin, M. Haertlein, V. T. Forsyth, L. Lindfors and M. Cárdenas, *ACS Nano*, 2021, **15**, 6709–6722.
33 S. Liu, Q. Cheng, T. Wei, X. Yu, L. T. Johnson, L. Farbiak and D. J. Siegwart, *Nat. Mater.*, 2021, **20**, 701–710.
34 J. Schindelin, I. Arganda-Carreras, E. Frise, V. Kaynig, M. Longair, T. Pietzsch, S. Preibisch, C. Rueden, S. Saalfeld, B. Schmid, J.-Y. Tinevez, D. J. White, V. Hartenstein, K. Eliceiri, P. Tomancak and A. Cardona, *Nat. Methods*, 2012, **9**, 676–682.
35 M. Medina-O'Donnell, K. Vega-Granados, A. Martinez, M. R. Sepúlveda, J. A. Molina-Bolívar, L. A. de Cienfuegos, A. Parra, F. J. Reyes-Zurita and F. Rivas, *J. Nat. Prod.*, 2023, **86**, 166–175.

36 L. Mei, S. He, L. Zhang, K. Xu and W. Zhong, *Org. Biomol. Chem.*, 2019, **17**, 939–944.
37 H. Maus, P. Müller, M. Meta, S. N. Hoba, S. J. Hammerschmidt, R. A. Zimmermann, C. Zimmer, N. Fuchs, T. Schirmeister and F. Barthels, *Chem. – Eur. J.*, 2023, **29**, e202301855.
38 Y. Yang, D. Zhang, M. Xu, J. Wang, J. Chen and L. Wang, *Monatsh. Chem.*, 2018, **149**, 1003–1008.
39 Z.-R. Lu and D. Sun, *Pharm. Res.*, 2025, **42**, 1065–1077.
40 K. Mrksich, M. S. Padilla and M. J. Mitchell, *Adv. Drug Delivery Rev.*, 2024, **214**, 115446.
41 X. Wang, H. Li, C. Chen and Z. Liang, *Smart Mol.*, 2025, **3**(4), e20240017, DOI: 10.1002/smo.20240017.
42 S. Kamble, S. Agrawal, S. Cherumukkil, V. Sharma, R. V. Jasra and P. Munshi, *ChemistrySelect*, 2022, **7**(1), e202103084.
43 J. Philipp, A. Dabkowska, A. Reiser, K. Frank, R. Krzysztoń, C. Brummer, B. Nickel, C. E. Blanchet, A. Sudarsan, M. Ibrahim, S. Johansson, P. Skantze, U. Skantze, S. Östman, M. Johansson, N. Henderson, K. Elvevold, B. Smedsrød, N. Schwierz, L. Lindfors and J. O. Rädler, *Proc. Natl. Acad. Sci. U. S. A.*, 2023, **120**, e2310491120.
44 K. Koitabashi, H. Nagumo, M. Nakao, T. Machida, K. Yoshida and K. Sakai-Kato, *Biochim. Biophys. Acta, Biomembr.*, 2021, **1863**, 183627.
45 L. Liu, J.-H. Kim, Z. Li, M. Sun, T. Northen, J. Tang, E. Mcintosh, S. Karve and F. DeRosa, *Nanoscale*, 2025, **17**, 11329–11344.
46 L. Zheng, S. R. Bandara, Z. Tan and C. Leal, *Proc. Natl. Acad. Sci. U. S. A.*, 2023, **120**, e2301067120.
47 H. Yu, J. Iscaro, B. Dyett, Y. Zhang, S. Seibt, N. Martinez, J. White, C. J. Drummond, S. Bozinovski and J. Zhai, *J. Am. Chem. Soc.*, 2023, **145**, 24765–24774.
48 S. A. Dilliard, Q. Cheng and D. J. Siegwart, *Proc. Natl. Acad. Sci. U. S. A.*, 2021, **118**, e2109256118.
49 H. Lv, S. Zhang, B. Wang, S. Cui and J. Yan, *J. Controlled Release*, 2006, **114**, 100–109.